

Seismic interferometry with neural networks

Hongyu Sun* and Laurent Demanet, Earth Resources Laboratory, Massachusetts Institute of Technology

SUMMARY

Under the assumptions of diffuse wavefields or energy equipartitioning, theoretical studies showed that the Green's function can be retrieved from the cross-correlation of ambient noise in seismic interferometry (SI). However, in practice, correlograms are not equal to the empirical Green's function since the assumptions for correlation-based SI are generally not satisfied in realistic situations. In the framework of supervised learning, we propose to train deep neural networks to overcome two limitations of correlation-based SI: the temporal limitation of passive recordings, and the spatial limitation of the random source distribution. Deep neural networks are trained to implicitly find the relationship between the empirical Green's function and the correlograms, and then used to extract the correct Green's function from ambient noise. The input of the network is correlograms (a virtual shot gather) and the desired output is the empirical Green's function (the active shot gather). Numerical examples show that a deep network aware of the source directionality (through a preliminary beamforming step) can help mitigate some of the challenges associated with inhomogeneous source distributions. In this work, all the numerical examples are based on the retrieval of P-wave reflections at exploration scales, and are conducted on synthetic data. Many precautions are taken to avoid the “learning crime” where the training and testing scenarios are too closely related. We use the CycleGAN architecture in all our numerical experiments.

INTRODUCTION

Seismic interferometry generally refers to the process of generating new seismic responses (Green's function retrieval) by correlating seismic noise recordings of different receivers (Schuster et al., 2004; Wapenaar and Fokkema, 2006). Since Aki (1957) proposed to use statistical properties of seismic noise to infer the Earth's structure, SI applications have ranged from crust and upper-mantle structure investigation (Yao et al., 2008), to natural resources exploration, to urban monitoring.

Claerbout (1968) pioneered the SI algorithm by autocorrelating a transmission seismogram to retrieve its reflection. Subsequently, the principle of correlation-based SI has been derived via normal-mode summation (Lobkis and Weaver, 2001), time reversal (Roux and Fink, 2003), representation theorems (Wapenaar, 2004) and stationary phase analysis (Snieder et al., 2006) by assuming that the ambient wavefield is equipartitioned.

The challenges of correlation-based SI mainly concern extending the theory to account for real-world noise and media (Curtis et al., 2006; Tsai, 2010; Fichtner, 2014). Correct retrieval of the Green's function relies on the prerequisite of uncorrelated

and homogeneously distributed noise sources in media without intrinsic losses. A strong localized source outside the stationary zones can cause spurious arrivals resulting from imperfect cancellations of nonphysical amplitudes (Snieder et al., 2008). However, natural noise sources are always correlated and cannot illuminate the region of interest from all sides equally. Also, seismic waves in real-world media can suffer from geometrical spreading and attenuation (hence lowered amplitudes). In addition, there is the issue of statistical stability – large deviations in the case of small sample size (here, short recording window).

In addition to cross-correlations, alternative methods for SI include: deconvolution (Vasconcelos and Snieder, 2008), multi-dimension deconvolution (Wapenaar et al., 2008), cross-coherence (Nakata et al., 2011) and coda wave interferometry (Snieder, 2004; Shapiro et al., 2005). More robust pre-processing and post-processing methods are proposed to enhance the reliability of Green's function extraction from cross-correlation, e.g., directional balancing (Curtis and Halliday, 2010) and iterative denoising (Zhang et al., 2015).

Deep learning (LeCun et al., 2015) enables neural networks with multiple layers to discover intricate structure from large data sets and learn high-level representations for reasonable prediction. Over the past few years, it was used in geophysics for solving inverse problems (Khoo and Ying, 2019), low frequency extrapolation (Sun and Demanet, 2020) and velocity model building (Araya-Polo et al., 2018; Zhang and Lin, 2020).

In passive data processing, researchers have leveraged machine learning in different ways. Clancy et al. (2018) use deep learning to measure the time lapse between two correlograms. Bharadwaj et al. (2020) design an autoencoder for time-lapse monitoring with passive seismic data. Viens and Van Houtte (2020) train an autoencoder to denoise noise correlation functions with a time resolution of 20 minutes. Zhang et al. (2020) extract dispersion curves from ambient noise correlations using deep learning. As for unsupervised learning, Viens and Iwata (2020) use clustering method to improve the quality of correlograms calculated via deconvolution. Seydoux et al. (2020) use unsupervised deep learning to distinguish between earthquake signals and background noises. Jakkampudi et al. (2020); Binder and Tura (2020); Stork et al. (2020) apply machine learning for signal detection from ambient noise under a classification framework.

To handle the practical challenges in SI applications, we propose to use supervised deep learning to extract the correct Green's function from ambient noise wavefields with limited recording duration and localized source distribution. We focus on retrieval of the Greens function at exploration scales. Specifically, we aim to retrieve reflected waves from ambient noise that agree with (here, simulated) active surveys. Direct mapping from noise to signal is optional but requires a careful design of the neural network. To relieve the difficulty of learning,

Seismic interferometry with neural networks

we use raw correlograms as input to the network, and train the latter to output reflections, i.e., seismic events from an active source. Numerical examples have shown that deep learning with proper setting can overcome the temporal limitation of noise recording length and spatial limitation of source distribution in correlation-based SI. We believe that seismic imaging with deep-learning-retrieved reflections from short noise recordings, and less-than-ideal source characteristics, offers an interesting new point of view for real-time monitoring.

DATA AND METHOD

Review of correlation-based interferometry

Correlation-based SI retrieves Green's function from N available passive measurements $u_{obs}(\mathbf{x}_A, t)$ and $u_{obs}(\mathbf{x}_B, t)$ using the relation (Wapenaar, 2004; Wapenaar and Fokkema, 2006):

$$\{G(\mathbf{x}_A, \mathbf{x}_B, t) + G(\mathbf{x}_A, \mathbf{x}_B, -t)\} * S(t) \approx \sum_i^N u_{obs}^i(\mathbf{x}_A, -t) * u_{obs}^i(\mathbf{x}_B, t). \quad (1)$$

Here, $G(\mathbf{x}_A, \mathbf{x}_B, \pm t)$ is the Green's function between positions \mathbf{x}_A and \mathbf{x}_B in a homogeneous lossless acoustic medium. $\pm t$ denotes the causal and acausal parts of the Green's function. $S(t)$ stands for the autocorrelation of the noise sources, and the asterisk denotes convolution.

The derivation of this relation relies on the assumption that ambient noise sources are uncorrelated and surround the area of interest from all directions. However, correlograms are not equal to Green's function when the assumption is not fulfilled. In addition to an amplitude error, artifacts will be introduced in the reconstructed signal due to the fact that the source locations do not constitute a closed surface (Snieder et al., 2006; Wapenaar, 2006; Thorbecke and Wapenaar, 2008).

Deep learning for seismic interferometry

We use deep learning to extract the correct Green's function from correlograms in a supervised manner to overcome the practical challenges of SI in imperfect situations: short recording time and inhomogeneous source distribution. The raw input \mathbf{x} of the neural network is virtual shot gathers (correlograms) and the active shot gathers serve as the desired output (label \mathbf{z}).

We collect both the training and test data sets from a synthetic data set simulated on several 2D models extracted from the 3D SEG/EAGE Overthrust Model (Aminzadeh et al., 1996). In total, we have one test model and 16 training models. Figure 1a and Figure 1b show the P-wave velocity of the test model and the training model I, respectively. We use the structural similarity image metric (SSIM, Wang et al. (2004)) to measure the similarity between a test model and a training model. Although it could be negative, the SSIM formula typically computes a continuous number between 0.0 and 1.0, where 1.0 corresponds to identical images and 0.0 corresponds to completely dissimilar images. Figure 1c shows the map of SSIM index between the test model and the training model I. Figure 1d shows the average SSIM index between the test model

and all the training models. The low similarity guarantees the suitability of the test dataset for evaluating the trained neural networks.

We follow the method in Thorbecke and Draganov (2011) to simulate the ambient noise recordings. The wavefields are simulated by solving the 2D acoustic wave equation in the time domain using the finite difference method. A perfectly matched layer (PML) is applied to the bottom, right and left boundary of each model, while a free surface condition is applied to the top of the model. With an interval of 40 m, 224 receivers are evenly placed from 520 m to 9480 m on the top of each model. With a sampling rate of 8 ms, we record 300 s passive data on the test model and 120 s passive data on the training model. During the total recording time, 1000 noise sources are triggered with random starting times at random locations. The amplitude and duration of these noise sources are random, but the maximum frequency of each noise source is 12 Hz.

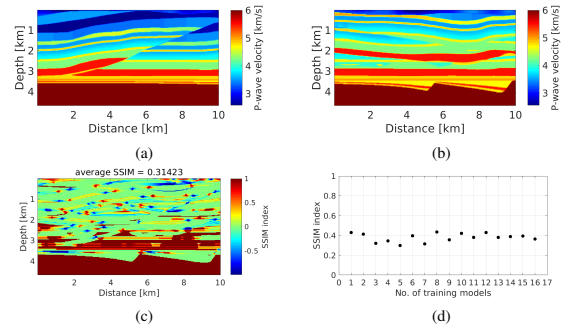


Figure 1: (a) Test model. (b) Training model I. (c) The map of SSIM index between the test model and training model I. (d) The average SSIM index between the test model with all the training models.

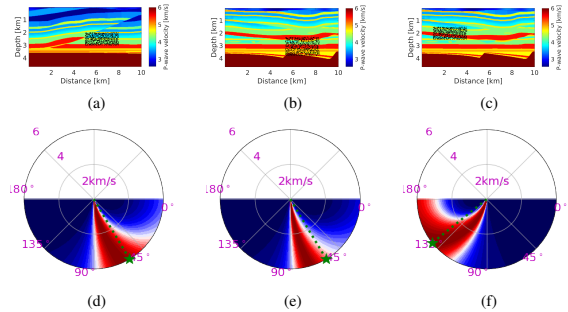


Figure 2: Comparison of (a) source locations on the test model, (b) the first choice and (c) the second choice of source locations on the training model I for simulating training datasets; (d)-(f) beamforming results of the noise recordings with source locations in (a)-(c), respectively.

To study the imperfect situation of inhomogeneous source distribution, we place all the noise sources in one part of the subsurface. Figure 2a shows the locations of 1000 random noise sources in the rectangular region of $5000 \text{ m} \leq x \leq 8000 \text{ m}$ and $2000 \text{ m} \leq z \leq 3000 \text{ m}$. To reduce the generalization gap, an

Seismic interferometry with neural networks

ideal training data set should have the same source distribution as the test data set. However, the source configuration of the test dataset is usually unknown in practice. Therefore, we determine the source directionality of the passive recordings using a beamforming method, and use the estimated source locations to simulate the training datasets when the sources are localized in the subsurface. Among the methods to estimate the angle of arrival, we choose MULTiple SIGNAL Classification (MUSIC, Schmidt (1986)) for its higher resolution compared with classical beamforming approaches. This paper only considers the estimation of a single quantity, the angle of the leading direction of incidence of the noise, to then inform the training step of the network by providing noise distributions calibrated on this single parameter. We do not attempt to match the complete beam pattern, although this could be an interesting direction for future research.

On the test model, the beamforming result (Figure 2d) reveals that the source direction ranges from 45° to 90° respect to the middle of the receiver array, which is roughly consistent with the true angle of the center of the source area indicated by the green star. To simulate a training dataset with a similar source direction as the test dataset, we randomly place 1100 sources in the rectangular region of $5330 \text{ m} \leq x \leq 8330 \text{ m}$ and $2300 \text{ m} \leq z \leq 3800 \text{ m}$ on each training model. The neural network is expected to achieve good performance when trained using the designed source configuration (Figure 2b). For comparison, we put sources in another region of each training model (Figure 2c) to investigate the importance of the prior knowledge of the source distribution. The beamforming result (Figure 2f) also shows that the source direction is very different from that on the test model.

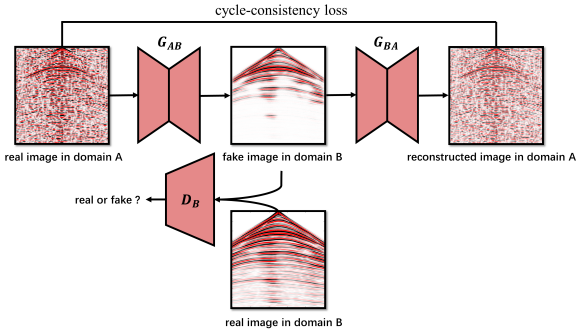


Figure 3: A cartoon flowchart of the CycleGAN used for reflection retrieval from ambient noise. The architecture contains two generators: G_{AB} and G_{BA} , and two discriminators: D_B and D_A . The network's input \mathbf{x} is a virtual shot gather in the domain A . Domain B contains the active shot gathers. The images in the domain A and B are aligned with the same virtual/active shot location.

We formulate reflection retrieval from ambient noise as an image-to-image translation problem using Cycle-Consistent Adversarial Networks (CycleGAN, Zhu et al. (2017)). CycleGAN is one of the most popular architectures for learning to translate an image from a source domain A to a target domain B . Figure 3 summarizes the flowchart of the CycleGAN. In our

application, the source domain A contains 2D images of the virtual shot gather and the target domain B is a collection of 2D images of the active shot gather. We train the CycleGAN using a training set of aligned images pairs. Both input \mathbf{x} and output \mathbf{y} have equivalent dimensions of $nt \times ntr$ where nt and ntr are numbers of recording points and receivers, respectively.

The CycleGAN contains two generators $G_{AB} : A \rightarrow B$ and $G_{BA} : B \rightarrow A$, and associated adversarial discriminators D_B and D_A . D_B encourages G_{AB} to generate images from domain A indistinguishable from domain B by training an adversarial loss. The loss and specific architectures of G_{AB} , G_{BA} , D_B , and D_A are the same as Zhu et al. (2017). During training, we use adaptive moment estimation (Adam, Kingma and Ba (2014)) to simultaneously update G_{AB} , G_{BA} , D_B , and D_A with a mini-batch of one. The learning rate is set as 2×10^{-5} .

The subsequent preprocessing steps are followed to generate each pair of images in the training and test data sets:

- The input \mathbf{x} is a virtual short gather (correlograms);
- The desired output \mathbf{z} (label) is the active shot gather generated by placing an active source at the position of the virtual source. Here we use a Ricker wavelet with 6 Hz dominate frequency and 12 Hz maximum frequency as the active source;
- Both the active and virtual shot gathers should be band-pass filtered to equalize the frequency components. Here both the active and virtual shot gathers have roughly the same frequency components so we omit this step;
- We taper the shot gathers with zero at the beginning of each time series using a time window of 0.16 s to remove the extreme large amplitude at the positions of the virtual/active shot locations;
- We normalize the input \mathbf{x} and label \mathbf{z} to $[-1, 1]$;

After preprocessing, we use each pair of the virtual and active shot gathers with the same shot location as the 2D images for the input and target of the CycleGAN. Specifically, with the time dimension of $nt = 496$ and the distance dimension of $ntr = 224$, the shot gather to be processed is 3.96 s in time and 8920 m in distance, respectively. As a result, for each case, we have a total of 3584 training image pairs (16 training models \times 224 shots per model) and 224 test image pairs (1 test model \times 224 shots per model). Furthermore, we retain the effect of the wavelet on the virtual and active shot gathers during training. Consequently, deconvolution of the source wavelet from the prediction of the neural networks is required to retrieve Green's function from reflections. The source wavelet can be approximated by the Ricker wavelet used in the simulation of the active-source common shot gather.

NUMERICAL RESULTS

After training with three epochs, Figure 4 compares the virtual shot gather, the active shot gather and the G_{AB} prediction where the virtual/active shot is located at $x = 6480 \text{ m}$ on the test model. Since the source distribution is not suitable

Seismic interferometry with neural networks

for correlation-based SI, many spurious events can be seen on the correlograms. Compared with the correlograms, the G_{AB} prediction (Figure 4d) generally shows good agreement with the active shot gather. However, deeper reflections have lower SNR and are challenging for the G_{AB} to detect and recover from correlograms. Without the prior knowledge of the source locations, the neural network loses its generalization ability among different source directions and creates more artifacts than the passive correlation (Figure 4c).

We use the test model (after smoothing the structure less than 1 km with a Gaussian filter) to migrate the virtual, G_{AB} predicted and active shot gathers to evaluate the performance of the passive recordings for seismic imaging. 112 shots with an interval of 80 m are migrated using the phase shift plus interpolation (PSPI) method (Gazdag and Sguazzero, 1984) shot-by-shot and then summed up for the final imaging results (Figure 5). Although some discrepancies exist in the near surface, imaging using the G_{AB} prediction (Figure 5d) removes many artifacts due to spurious events compared to that using the raw virtual shot gathers. In particular, imaging using the G_{AB} prediction is less contaminated by multiples compared with the result using the active shot gathers. Although we trained the neural network with data sets that contain multiples, the surface-related multiples arrive at later time and thus have less SNR compared to the primaries on the virtual shot gathers. The trained G_{AB} predicts fewer multiples and thus seismic imaging using the predicted gathers has fewer artifacts due to multiples.

Since the source distribution is inhomogeneous, the left area without sources is not illuminated and thus is not imaged by either type of passive data. Most reflectors on the image with the predicted shot gathers from the similar source direction (Figure 5d) are comparable to the one using the active shot gathers (Figure 5b). In contrast, although the overall image in Figure 5c shows the layered structure of the subsurface, the positions of several major reflectors are wrong. Moreover, the shallow structure is not accurately imaged using the predicted shot gathers from the different source distribution. The comparison of the imaging results in Figure 5c and Figure 5d demonstrates that the prior knowledge of the source locations is helpful when dealing with passive recordings from a localized source distribution.

CONCLUSIONS

We propose to use supervised learning to handle the practical challenges of seismic interferometry in realistic situations. By substituting ambient noise for an active source, we train deep neural networks to reconstruct the reflections from correlograms. To overcome the temporal limitation of the noise recording length, the neural networks are trained to retrieve reflections from only 300 s passive measurements. To overcome the spatial limitation of source distribution, the neural networks are trained on noise data generated from a directional source distribution. Numerical examples demonstrate that deep learning can help with seismic interferometry to extract reasonably accurate signals from ambient noise in realistic situations. Instead of simply estimating travel times or

image reflectors from ambient noise, the retrieved reflections may be used in seismic imaging with the full Green's function. The new technology may help with near real-time monitoring of the Earth's dynamics in a wide ranges of areas, for example, urban environments.

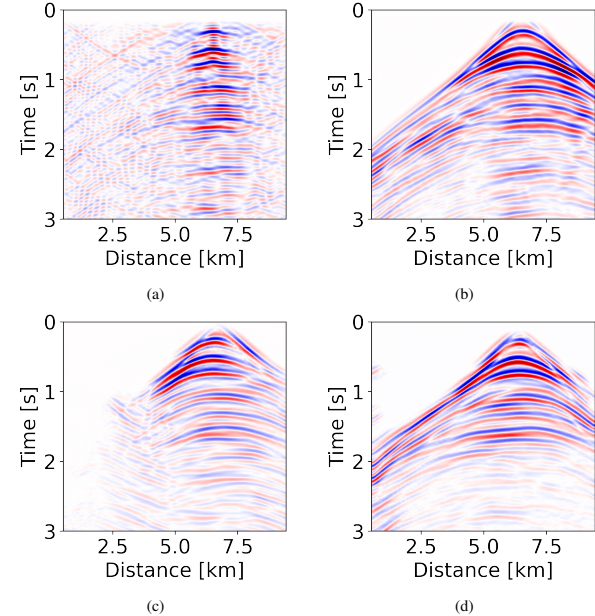


Figure 4: Comparison among (a) the virtual shot gather, (b) the active shot gather, (c) the predicted shot gather by the G_{AB} trained with different and (d) similar source distributions.

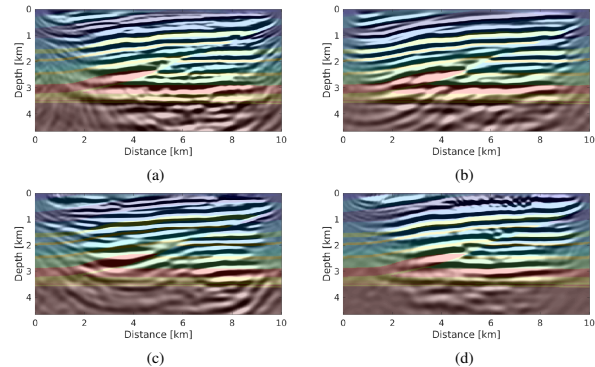


Figure 5: Comparison of prestack depth migration results using (a) virtual shot gathers, (b) active shot gathers, (c) predicted shot gathers by the G_{AB} trained with different and (d) similar source distributions.

ACKNOWLEDGMENTS

The authors thank Total SA for support. Laurent Demanet is also supported by AFOSR grant FA9550-17-1-0316. Hongyu Sun acknowledges SEG scholarships for funding. The authors thank Zhilong Fang from MIT for helpful discussions.

Seismic interferometry with neural networks

REFERENCES

- Aki, K., 1957, Space and time spectra of stationary stochastic waves, with special reference to microtremors: *Bulletin of the Earthquake Research Institute*, **35**, 415–456.
- Aminzadeh, F., N. Burkhard, J. Long, T. Kunz, and P. Duclos, 1996, Three dimensional seg/eaeg modelsan update: *The Leading Edge*, **15**, 131–134.
- Araya-Polo, M., J. Jennings, A. Adler, and T. Dahlke, 2018, Deep-learning tomography: *The Leading Edge*, **37**, 58–66.
- Bharadwaj, P., M. Li, and L. Demanet, 2020, Symae: an autoencoder with embedded physical symmetries for passive time-lapse monitoring, in *SEG Technical Program Expanded Abstracts 2020*: Society of Exploration Geophysicists, 1586–1590.
- Binder, G., and A. Tura, 2020, Convolutional neural networks for automated microseismic detection in downhole distributed acoustic sensing data and comparison to a surface geophone array: *Geophysical Prospecting*, **68**, 2770–2782.
- Claerbout, J. F., 1968, Synthesis of a layered medium from its acoustic transmission response: *Geophysics*, **33**, 264–269.
- Clancy, J., L. Demanet, J. Helland, and Z. Xu, 2018, Deep learning for making sense of ambient seismic noise: *AGU FM*, **2018**, S13B–03.
- Curtis, A., P. Gerstoft, H. Sato, R. Snieder, and K. Wapenaar, 2006, Seismic interferometryturning noise into signal: *The Leading Edge*, **25**, 1082–1092.
- Curtis, A., and D. Halliday, 2010, Directional balancing for seismic and general wavefield interferometry: *Geophysics*, **75**, SA1–SA14.
- Fichtner, A., 2014, Source and processing effects on noise correlations: *Geophysical Journal International*, **197**, 1527–1531.
- Gazdag, J., and P. Sguazzero, 1984, Migration of seismic data by phase shift plus interpolation: *Geophysics*, **49**, 124–131.
- Jakkampudi, S., J. Shen, W. Li, A. Dev, T. Zhu, and E. R. Martin, 2020, Footstep detection in urban seismic data with a convolutional neural network: *The Leading Edge*, **39**, 654–660.
- Khoo, Y., and L. Ying, 2019, Switchnet: a neural network model for forward and inverse scattering problems: *SIAM Journal on Scientific Computing*, **41**, A3182–A3201.
- Kingma, D. P., and J. Ba, 2014, Adam: A method for stochastic optimization: arXiv preprint arXiv:1412.6980.
- LeCun, Y., Y. Bengio, and G. Hinton, 2015, Deep learning: *nature*, **521**, 436–444.
- Lobkis, O. I., and R. L. Weaver, 2001, On the emergence of the greens function in the correlations of a diffuse field: *The Journal of the Acoustical Society of America*, **110**, 3011–3017.
- Nakata, N., R. Snieder, T. Tsuji, K. Larner, and T. Matsuoka, 2011, Shear wave imaging from traffic noise using seismic interferometry by cross-coherenceshear wave imaging from traffic noise: *Geophysics*, **76**, SA97–SA106.
- Roux, P., and M. Fink, 2003, Greens function estimation using secondary sources in a shallow water environment: *The Journal of the Acoustical Society of America*, **113**, 1406–1416.
- Schmidt, R., 1986, Multiple emitter location and signal parameter estimation: *IEEE transactions on antennas and propagation*, **34**, 276–280.
- Schuster, G., J. Yu, J. Sheng, and J. Rickett, 2004, Interferometric/daylight seismic imaging: *Geophysical Journal International*, **157**, 838–852.
- Seydoux, L., R. Balestro, P. Poli, M. De Hoop, M. Campillo, and R. Baraniuk, 2020, Clustering earthquake signals and background noises in continuous seismic data with unsupervised deep learning: *Nature communications*, **11**, 1–12.
- Shapiro, N. M., M. Campillo, L. Stehly, and M. H. Ritzwoller, 2005, High-resolution surface-wave tomography from ambient seismic noise: *Science*, **307**, 1615–1618.
- Snieder, R., 2004, Extracting the greens function from the correlation of coda waves: A derivation based on stationary phase: *Physical Review E*, **69**, 046610.
- Snieder, R., K. Van Wijk, M. Haney, and R. Calvert, 2008, Cancellation of spurious arrivals in greens function extraction and the generalized optical theorem: *Physical Review E*, **78**, 036606.
- Snieder, R., K. Wapenaar, and K. Larner, 2006, Spurious multiples in seismic interferometry of primaries: *Geophysics*, **71**, SI111–SI124.
- Stork, A. L., A. F. Baird, S. A. Horne, G. Naldrett, S. Lapins, J.-M. Kendall, J. Wookey, J. P. Verdon, A. Clarke, and A. Williams, 2020, Application of machine learning to microseismic event detection in distributed acoustic sensing data: *Geophysics*, **85**, KS149–KS160.
- Sun, H., and L. Demanet, 2020, Extrapolated full-waveform inversion with deep learning: *Geophysics*, **85**, R275–R288.
- Thorbecke, J., and K. Wapenaar, 2008, Analysis of spurious events in seismic interferometry, in *SEG Technical Program Expanded Abstracts 2008*: Society of Exploration Geophysicists, 1415–1420.
- Thorbecke, J. W., and D. Draganov, 2011, Finite-difference modeling experiments for seismic interferometry: *Geophysics*, **76**, H1–H18.
- Tsai, V. C., 2010, The relationship between noise correlation and the green's function in the presence of degeneracy and the absence of equipartition: *Geophysical Journal International*, **182**, 1509–1514.
- Vasconcelos, I., and R. Snieder, 2008, Interferometry by deconvolution: Part 1theory for acoustic waves and numerical examples: *Geophysics*, **73**, S115–S128.
- Viens, L., and T. Iwata, 2020, Improving the retrieval of offshore-onshore correlation functions with machine learning: *Journal of*

Seismic interferometry with neural networks

- Geophysical Research: Solid Earth, **125**, e2020JB019730.
- Viens, L., and C. Van Houtte, 2020, Denoising ambient seismic field correlation functions with convolutional autoencoders: Geophysical Journal International, **220**, 1521–1535.
- Wang, Z., A. C. Bovik, H. R. Sheikh, and E. P. Simoncelli, 2004, Image quality assessment: from error visibility to structural similarity: IEEE transactions on image processing, **13**, 600–612.
- Wapenaar, K., 2004, Retrieving the elastodynamic green's function of an arbitrary inhomogeneous medium by cross correlation: Physical review letters, **93**, 254301.
- , 2006, Green's function retrieval by cross-correlation in case of one-sided illumination: Geophysical Research Letters, **33**.
- Wapenaar, K., and J. Fokkema, 2006, Greens function representations for seismic interferometry: Geophysics, **71**, SI33–SI46.
- Wapenaar, K., J. van der Neut, and E. Ruigrok, 2008, Passive seismic interferometry by multidimensional deconvolution: Geophysics, **73**, A51–A56.
- Yao, H., C. Beghein, and R. D. Van Der Hilst, 2008, Surface wave array tomography in se tibet from ambient seismic noise and two-station analysis-ii. crustal and upper-mantle structure: Geophysical Journal International, **173**, 205–219.
- Zhang, P., L.-G. Han, Q. Liu, Y.-H. Zhang, and X. Chen, 2015, Interpolation of seismic data from active and passive sources and their joint migration imaging: Chinese Journal of Geophysics-Chinese Edition, **58**, 1754–1766.
- Zhang, X., Z. Jia, Z. E. Ross, and R. W. Clayton, 2020, Extracting dispersion curves from ambient noise correlations using deep learning: IEEE Transactions on Geoscience and Remote Sensing.
- Zhang, Z., and Y. Lin, 2020, Data-driven seismic waveform inversion: A study on the robustness and generalization: IEEE Transactions on Geoscience and Remote Sensing.
- Zhu, J.-Y., T. Park, P. Isola, and A. A. Efros, 2017, Unpaired image-to-image translation using cycle-consistent adversarial networks: Proceedings of the IEEE international conference on computer vision, 2223–2232.